# Evidence of Ultrashort Orbital Diffusion Lengths in Heavy Metals Revealed by Terahertz Emission Spectroscopy

Tongyang Guan<sup>1,2,§</sup>, Jiahao Liu<sup>1,2,§</sup>, Wentao Qin<sup>1,2</sup>, Yongwei Cui<sup>1,2</sup>, Shunjia Wang<sup>1,2</sup>, Yizheng Wu<sup>1,2,\*</sup>, Zhensheng Tao<sup>1,2,\*</sup>

<sup>1</sup>State Key Laboratory of Surface Physics and Key Laboratory of Micro and Nano Photonic Structures (MOE), Department of Physics, Fudan University, Shanghai 200433, P R China.

<sup>2</sup>Shanghai Key Laboratory of Metasurfaces for Light Manipulation, Fudan University, Shanghai 200433, P R China.

§ These authors contributed equally to this work.

\* Corresponding authors: wuyizheng@fudan.edu.cn; zhenshengtao@fudan.edu.cn.

#### **Abstract**

The orbital angular momentum of electrons offers a promising, yet largely unexplored, degree of freedom for ultrafast, energy-efficient information processing. As the foundation of orbitronics, understanding how orbital currents propagate and convert into charge currents is essential – but remains elusive due to the challenge in disentangling orbital and spin dynamics in ultrathin films. While theoretical studies predict that orbital transport is constrained to sub-atomic-layer scales in materials, recent experiments have reported exceptionally long orbital diffusion lengths, posing a fundamental contradiction. To address this, we combine terahertz emission spectroscopy with a wedge-sample platform to systematically investigate spin and orbital transport in heavy metals with sub-nanometer resolution. Our high-resolution measurements access the previously unexplored ultrathin regime (<3 nm), uncovering anomalous behaviors that directly challenge the prevailing interpretations of long-range orbital transport. Interface-sensitive control experiments further rule out interfacial orbital-to-charge conversion as the dominant mechanism, supporting the bulk inverse orbital Hall effect as the primary conversion process. These findings address a central controversy in orbitronics and provide key insights into orbital transport and conversion mechanisms.

Orbitronics is an emerging field that seeks to control and manipulate electronic orbital angular momentum (L) in solids, offering new avenues for information processing and magnetic control<sup>1-4</sup>. Compared to spin angular momentum (S), which underpins conventional spintronics<sup>5-7</sup>, orbital degrees of freedom can carry larger angular momentum. This enables more efficient torques on magnetic moments, a possibility that has been both theoretically predicted<sup>8-10</sup> and experimentally demonstrated<sup>11-15</sup>.

Several experiments have reported long-range orbital transport, suggesting that orbital currents – flows of L – can propagate over tens of nanometers and drive magnetic excitation far from material interfaces  $^{11,15-17}$ . In particular, femtosecond laser-induced terahertz emission spectroscopy has revealed orbital diffusion lengths ranging from 9 nm to 80 nm in non-magnetic materials  $^{18-20}$ , supporting interpretations based on interfacial orbital-to-charge conversion via the inverse orbital Rashba-Edelstein effect (IOREE)  $^{18-21}$ .

However, these experimental claims stand in sharp contrast to recent theoretical predictions. While long orbital transport has been proposed under specific momentum-space conditions<sup>22</sup>, recent first-principles calculations indicate that orbital propagation is fundamentally constrained by crystal symmetry, limiting orbital diffusion length to sub-atomic-layer scales<sup>23–25</sup>. This contradiction stems from the fact that current electrical<sup>12,16,17,26</sup> or optical<sup>11,15,18–20</sup> probes cannot unambiguously distinguish between spin and orbital contributions. While X-ray<sup>27</sup> and electron<sup>28</sup> magnetic circular dichroism may offer selective sensitivity to S and L, direct observation of pure orbital transport

remain elusive. This raises a fundamental question: are the previously reported longrange orbital transport signals genuinely due to L, or are they artifacts arising from unresolved spin-orbital entanglement?

In light of theoretical predictions that orbital transport is ultrashort<sup>23–25</sup>, it is essential to examine orbital transport in the ultrathin regimes (<3 nm) with subnanometer precision, where orbital diffusion is expected to be most constrained. Yet, this critical parameter space has remained unexplored in previous experimental studies.

In this work, we systematically investigate orbital and spin transport in heavy metals (HMs) using terahertz emission spectroscopy on wedge-shaped HM|ferromagnet (FM) heterostructures. The wedge-sample platform provides subnanometer spatial resolution and enables continuous thickness scanning, allowing access to the previously unexplored ultrathin regime (<3 nm). Our high-resolution measurements uncover anomalous behaviors in this regime that directly challenge prevailing interpretations of long-range orbital transport.

Specifically, in W|Ni heterostructures, we observe a pronounced non-monotonic dependence of terahertz emission on W thickness and a polarity reversal in the ultrathin regime, providing evidence that orbital diffusion lengths ( $\lambda_L$ ) are significantly shorter than spin diffusion lengths ( $\lambda_S$ ). Furthermore, our high-resolution, interface-sensitive control experiments further *rule out* the dominant roles of interfacial conversion mechanisms, supporting a bulk-origin scenario mediated by the inverse orbital Hall effect (IOHE) and inverse spin Hall effect (ISHE). A multi-component terahertz emission model is established and enables semi-quantitative extraction of  $\lambda_L$  across

several HMs (W, Ta, and Pt), consistently showing  $\lambda_L < \lambda_S$ . These findings resolve a key controversy in orbitronics and establish a robust experimental framework for disentangling spin and orbital dynamics at the nanoscale.

# **Experimental Principle**

Figure 1 illustrates the fundamental principle of our experiment. Upon excitation by a femtosecond laser pulse, ultrafast spin (js) and orbital (jt) currents are simultaneously generated in the FM layer of a HM|FM heterostructure. The S and L polarizations are aligned by an external magnetic field (H), and the resulting currents propagate along the out-of-plane (z) direction into the adjacent HM layer, where spin-to-charge and orbital-to-charge conversion processes give rise to in-plane charge currents that emit terahertz radiation.

To disentangle spin and orbital contributions, we selected FM and HM materials with distinct current-generation and conversion characteristics. Ni and Fe are selected as FM metals due to their high efficiency in generating orbital and spin currents, respectively<sup>29,30</sup>. For HM layers, we employ W, Ta, and Pt, which possess distinct signs of spin ( $\gamma_{SH}$ ) and orbital ( $\gamma_{OH}$ ) Hall angles<sup>9,31,32</sup>, as well as differing spin and orbital diffusion lengths ( $\lambda_L$  and  $\lambda_S$ ).

To achieve sub-nanometer thickness resolution and continuous thickness scanning, we fabricated wedge-shaped heterostructures where the HM thickness ( $d_{HM}$ , HM=W, Ta, Pt) varies continuously along the in-plane (x) direction, with a thickness gradient of ~1.6 nm/mm (Fig. 1). The FM-layer thickness ( $d_{FM}$ , FM=Ni, Fe) is fixed at 5 nm. By translating the sample in 0.1 mm steps along the x direction, we scan  $d_{HM}$  with a

resolution of  $\sim$ 0.16 nm, defined by the laser spot radius of  $\sim$ 50  $\mu$ m. Terahertz signals generated within the laser excitation area are detected via free-space electro-optic sampling<sup>33,34</sup>.

The wedge-shaped samples offer two key advantages: (i) it enables terahertz emission measurements with continuous sampling of  $d_{\rm HM}$  at sub-nanometer resolution, and (ii) it mitigates ambiguities associate with growth-condition variations in different samples. To further validate the reliability of our wedge-based measurements, we compared the results with those obtained from discrete thin-film samples with calibrated  $d_{\rm HM}$ . As shown in Supplementary Materials (SM) Fig. S3, the two sets of measurements are in excellent agreement, confirming the accuracy and robustness of our methodology.

Further details about sample preparation, characterization, and experimental setups are provided in the Methods and SM Section S1 and S2.

## Terahertz Signals from the W|Ni and Ni|W heterostructures

Figure 2 presents terahertz emission measurements from wedged-shaped W|Ni and Ni|W heterostructures. For comparison, we also include their Fe-based counterparts, W|Fe and Fe|W. Throughout this manuscript, "HM|FM" denotes the growth sequence of the heterostructure on the substrate, with the HM layer deposited first, followed by the FM layer. For clarity, the SiO<sub>2</sub> buffer and capping layers are omitted from the notation unless otherwise specified.

Figure 2a show selected terahertz waveforms from W(5)|Ni, W(0.8)|Ni, and W(5)|Fe (thickness in parentheses are in nanometers). The corresponding Ni|W and

Fe|W signals are shown in Fig. 2b. In W|Fe, the terahertz polarity is consistent with the spin Hall angle ( $\gamma_{SH}$ ) of W and opposite to that of Pt|Fe, indicating that terahertz generation is predominantly driven by spin currents via ISHE<sup>35–37</sup>. In Fe|W, the polarity is reversed due to the opposite stacking order, as expected.

In contrast, both W(0.8)|Ni and Ni|W(0.8) exhibit terahertz polarities at t=0 opposite to their Fe-counterparts, while those from W(5)|Ni and Ni|W(5) become aligning with W|Fe and Fe|W, respectively (Figs. 2a-b). This clear polarity reversal in W|Ni and Ni|W as a function of W thickness suggests more complex emission dynamics beyond conventional spintronic emitters.

Our high-resolution measurements further reveal the full evolution of terahertz emission with W thickness in details. In Figs. 2e-h, we present two-dimensional plots of terahertz waveforms as a function of  $d_W$ , with the corresponding amplitudes extracted at t=0 plotted in Figs. 2c-d. For the Fe-based samples, the amplitude increases with  $d_W$  and peaks around  $d_W\approx 3$  nm, consistent with the characteristic behavior of spintronic emitters<sup>37,38</sup>. Fitting the amplitude trend with the diffusive transport model<sup>37</sup> yields a spin diffusion length in W of ~2.20 nm (see below).

In stark contrast, both W|Ni and Ni|W exhibit a previously unresolved, non-monotonic thickness dependence in the ultrathin regime ( $d_W$ <3 nm), characterized by a pronounced peak near  $d_W$ ≈0.8 nm, followed by a deep minimum and polarity reversal between 2 - 3 nm. We note that these features are inconsistent with the long orbital diffusion lengths inferred in prior studies<sup>18</sup> and indicate more complex underlying dynamics.

To further clarify these findings – and in particular, to address the apparent contradiction with a prior study<sup>18</sup> reporting opposite terahertz polarities between Ni|W and Py|W when  $d_W>3$  nm – we compare the terahertz waveforms in greater detail (Fig. 2a-b). Our measurements reproduce the previously reported "opposite polarity" between Ni|W and Fe|W in the thick-W regime, with Ni|W(5) exhibiting a more pronounced negative peak near  $t\approx0.3$  ps (Fig. 2b). However, the high-resolution data reveal two key features that were not resolved in the earlier study:

- (i) For  $d_W < 2.8$  nm, both W(0.8)|Ni and Ni|W(0.8) show terahertz polarities opposite to their Fe-based counterparts. As  $d_W$  crosses 2.8 nm, both signal polarities at t=0 reverse, making them aligning with the Fe-based signals (Fig. 2g, h). The difference is that, in Ni|W, this polarity reversal is accompanied by a pronounced phase shift (Fig. 2g), more dramatic than in W|Ni (Fig. 2e), which effectively enhances the negative peak near  $t\approx 0.3$  ps. This waveform distortion accounts for the previously reported "opposite polarity"<sup>18</sup>.
- (ii) The phase shift in Ni|W is localized around the intensity minimum at  $d_W\approx 2-3$  nm (Fig. 2g and i), suggesting destructive interference between components of opposite polarity.

Crucially, despite the waveform and phase differences, both stacking orders – Ni|W and W|Ni – exhibit identical intensity features: a peak at ~0.8 nm and a minimum around 2-3 nm (Fig. 2i), indicating a common underlying mechanism independent of stacking order.

A detailed comparison with the results of Ref. 18 is provided in SM Section S4.

Notably, the high-resolution sampling enabled by our wedge-sample approach reveals key features in the ultrathin regime ( $d_W < 3$  nm) that were previously inaccessible, calling for a reassessment of the key interpretations in prior studies.

# **Exclusion of Interfacial Mechanisms**

The observed polarity reversal when  $d_W < 3$  nm in both W|Ni and Ni|W heterostructures relative to their Fe-based counterparts (Figs. 2c–d) strongly suggests the emergence of orbital contributions in the ultrathin regime. The sharp intensity rise below  $d_W \approx 0.8$  nm appears to suggest an interfacial orbital-to-charge conversion mechanism. Indeed, previous studies have proposed the IOREE as the dominant orbital-to-charge conversion mechanism in several systems<sup>18–21</sup>. In particular, Ref. 18 attributed the terahertz signal in Ni|W to the IOREE occurring at the buried W|SiO<sub>2</sub> interface, with the  $d_W$ -dependent time delays in terahertz peaks interpreted as the orbital transport time toward that interface.

In addition to the orbital-conversion mechanisms, the inverse spin Rashba-Edelstein effect (ISREE) could also contribute to terahertz emission, wherein spinpolarized currents are converted to in-plane charge currents at interfaces with strong spin-orbit coupling<sup>39,40</sup>.

Given that our measurements uncover previously unresolved anomalous features when  $d_W$ <3 nm, it is essential to critically re-evaluate the contribution of interfacial mechanisms in this thickness range. To this end, we conduct a series of control experiments by inserting a 1-nm Cu-spacer layer at either the W|Ni or SiO<sub>2</sub>|W interface in wedge-shaped W|Ni heterostructures. This approach intentionally disrupts potential

interfacial conversion channels, including the ISREE and IOREE (Fig. 3a). Similar approaches have been employed to resolve interfacial spin-to-charge conversion processes in prior studies<sup>41</sup>.

In Fig. 3b, we compare the terahertz signals from three configurations: (i) the reference sample  $SiO_2|W(0.7)|Ni$ , (ii)  $SiO_2|W(0.7)|Cu(1)|Ni$  with 1-nm Cu inserted at the W|Ni interface, and (iii)  $SiO_2|Cu(1)|W(0.7)|Ni$  with 1-nm Cu inserted at the  $SiO_2|W$  interface. Importantly, both the amplitude and waveform remain essentially unchanged upon Cu insertion at either interface. In Fig. 3c, we further present the terahertz amplitudes as a function of  $d_W$  for all the three configurations. Notably, all the samples exhibit a consistent trend: a positive terahertz signal for  $d_W$ <3 nm, peaking around  $d_W$ <0.7-0.8 nm, followed by an amplitude decrease with increasing  $d_W$ . The persistence of both signal strength and its  $d_W$ -dependence, despite disruption of the original interfaces by Cu insertion, essentially *rule out* the interfacial mechanisms, including the IOREE and ISREE, as the dominant mechanisms of the observed terahertz emission.

It is important to note that, while the Cu-layer insertion disrupts the original interfaces (SiO<sub>2</sub>|W and W|Ni), it inevitably introduces new interfaces, i.e. SiO<sub>2</sub>|Cu, Cu|W, W|Cu, and Cu|Ni, which could possibly generate terahertz emission. However, the persistence of the signal increase for  $d_W$ <0.8 nm across all the configurations (Fig. 3c) effectively rules out dominant contributions from these interfaces.

First, this signal increase rules out the  $SiO_2|Cu$  and Cu|Ni interfaces as dominant contributors, because these interfaces are detached from W. If either were responsible for the emission, increasing  $d_W$  would be expected to suppress the signal amplitude, via

orbital current blocking or electrical shunting, contrary to what we observe.

Second, if the IOREE or the ISREE occurred at the Cu|W or W|Cu interfaces, then reversing the interface orientation (i.e. SiO<sub>2</sub>|Cu|W|Ni vs. SiO<sub>2</sub>|W|Cu|Ni) should lead to opposite terahertz polarities. Yet, both configurations exhibit identical polarity and amplitude trends (Figs. 3b), further excluding the interfacial mechanisms at these interfaces as dominant effects.

Taken together, these findings clearly *rule out* interfacial mechanisms behind the observed terahertz emission in W|Ni. This conclusion is further reinforced by additional control experiments involving the insertion of a 2-nm Cu layer and a 1-nm Al layer. In both cases, the characteristic peak in terahertz amplitude when  $d_W < 3$  nm persists, indicating that the key features of the emission are robust against different spacer materials and interfacial configurations. Full experimental details and data are provided in SM Section S5.

In addition to the amplitude changes, previous studies also reported large time delays (>80 fs) in the terahertz signal with increasing  $d_W$ , interpreted as orbital-current propagation across W to the distant W|SiO<sub>2</sub> interface, ~20 nm away<sup>18</sup>. Such an interpretation would imply progressive time delays with increasing  $d_W$ . However, our high-resolution measurements show negligible shifts in the terahertz peak positions for  $d_W$ >5 nm in both W|Ni and Ni|W samples (Fig. 3d).

Significant time shifts do appear for  $2.0 \text{ nm} < d_W < 3.5 \text{ nm}$ , coinciding precisely with the region where the terahertz amplitude reaches minimum (Figs. 2c and e). Notably, such time delays are absent in other heterostructures, such as Ta|Ni and Pt|Ni, where no

amplitude minimum is observed (see below). This correlation suggests that the time delays are not a result of the orbital-transport time through HM, but rather arise from destructive interference between multiple contributions with opposite polarities and nontrivial phase shifts. These observations strongly support a mechanism involving coherent superposition of spin and orbital currents, rather than delayed interfacial conversion. A more detailed analysis of the time shifts is provided in Supplementary Section S6.

#### Disentangling Spin and Orbital Contributions: A Qualitative Analysis

With the interfacial mechanisms excluded, we resort to the bulk-origin mechanisms, including the ISHE and IOHE, in W. The pronounced amplitude minimum at  $d_W\approx 2\text{--}3$  nm, consistently observed in both W|Ni and Ni|W (Fig. 2i), indicates destructive interference between two dominant contributions of opposite polarity. This observation is consistent with the fact that the spin ( $\gamma_{SH}$ ) and orbital Hall ( $\gamma_{OH}$ ) angles have opposite signs in W, where  $\gamma_{SH}<0$  and  $\gamma_{OH}>0^{9,31,32}$ . Thus, both the amplitude minimum and the accompanying phase shifts near  $d_W\approx 2.8$  nm can be interpreted as the interference between spin- and orbital-originated currents with opposite signs and nontrivial phase offsets.

Further examining the polarity trends, at large W thicknesses ( $d_W>3$  nm), the terahertz polarity of W|Ni matches with that of W|Fe (Fig. 2a), suggesting that spin-to-charge conversion via ISHE dominates in the thick-W regime. Conversely, at ultrathin W layers ( $d_W<3$  nm), the polarity reverses, suggesting that the IOHE becomes dominant in this regime. This crossover behavior at  $d_W\approx2.8$  nm thus indicates that the orbital

diffusion length ( $\lambda_L$ ) is shorter than the spin diffusion length ( $\lambda_S$ ) in W, a conclusion that stands in stark contrast to previous reports<sup>18</sup>.

# Disentangling Spin and Orbital Contributions: A Semi-quantitative Model

Our experimental results in the ultrathin regime reveal terahertz emission behaviors that deviate from conventional spintronic emitters, calling for a quantitative framework to disentangle spin and orbital contributions.

We begin by noting that terahertz emission can be observed in the absence of the W layer ( $d_W$ =0 in Fig. 2e), indicating that the ferromagnetic Ni layer itself contributes to the signal. This contribution can be attributed to the anomalous Hall effect  $(AHE)^{20,42,43}$  and magnetic dipole emission  $(MDE)^{44-46}$ , and must be accounted for in any realistic model (see SM Section S3).

To enable quantitative comparisons, we develop a multi-component terahertz emission model (MC-TEM) by extending the well-established diffusion model<sup>37</sup>, which has been widely used in analyzing thickness-dependent terahertz emission in various spintronic emitters<sup>38,47,48</sup>. While a rigorous theoretical framework for orbital transport remains elusive, we adopt a pragmatic approach by modeling orbital currents using the same diffusive formalism developed for spin currents. This approach enables a meaningful, semi-quantitative comparison between spin and orbital diffusion lengths. Within this context, the MC-TEM yields an effective orbital diffusion length ( $\lambda_L^{\rm eff}$ ), without resolving additional complex processes, such as orbital-to-spin conversion<sup>25,49</sup>.

It is important to note that our central conclusion, that the orbital diffusion lengths in HMs are shorter than their spin diffusion lengths, is supported directly by

experimental observations and does not rely solely on the MC-TEM model. The purpose of the MC-TEM model is to offer a minimal yet effective framework to compare spin and orbital diffusion lengths on a semi-quantitative basis.

Details of the MC-TEM are provided in Methods. Briefly, the total terahertz emission is modeled as a superposition of three components:

 $E(t, d_{\text{HM}}) = A_S(d_{\text{HM}})\mathcal{E}_S(t) + A_L(d_{\text{HM}})\mathcal{E}_L(t) + A_{\text{Ni}}(d_{\text{HM}})\mathcal{E}_{\text{Ni}}(t),$ 

(1)

where the first two terms represent the spin and orbital contributions in the HM, and the third term accounts for the emission from the ferromagnetic Ni layer. Each term is decomposed into a thickness-dependent amplitude 
$$A_m$$
 and a thickness-independent

waveform  $\mathcal{E}_m$  (m=S, L, and Ni), supported by our experimental observations (see

Methods).

The spin  $(A_S)$  and orbital  $(A_L)$  amplitudes are modeled using the diffusive transport equations that incorporate optical absorption, interfacial current reflections, and electrical shunting effects<sup>37</sup>. For the Ni-layer amplitude  $A_{Ni}$ , since the Ni thickness is fixed in all samples, we treat the laser-excited Ni layer as a constant current source, with increasing  $d_W$  suppressing its contribution via enhanced optical attenuation and electrical shunting.

The spin- and Ni-layer-related waveforms,  $\mathcal{E}_S(t)$  and  $\mathcal{E}_{Ni}(t)$ , are directly extracted from the experimental data. The orbital waveform  $\mathcal{E}_L(t)$  is modeled by applying a carrier-envelope phase (CEP) shift  $\Delta \varphi$  to the spin waveform (see Methods):

$$\mathcal{E}_L(t) = \mathcal{E}_S(t)e^{i\Delta\varphi} + c.c., \tag{2}$$

with  $\Delta \varphi$  assumed to be thickness-independent.

Most variables in the MC-TEM are determined either by reference databases or by direct measurements (see Methods and SM Section S7). In particular, by setting  $A_L$ =0 and  $A_{\rm Ni}$ =0, the MC-TEM reduces to the established framework for spintronic emitters, which enables the extraction of spin diffusion lengths  $\lambda_S$  from the Fe-based heterostructures (see Figs. 2c and d). Consequently, for each HM|Ni sample, only 4 independent fitting parameters remain: the effective orbital diffusion length in HM ( $\lambda_L^{\rm eff}$ ), the spin and orbital amplitude coefficients ( $\tilde{A}_S$  and  $\tilde{A}_L$ ), and the CEP offset ( $\Delta \varphi$ ). Notably,  $\tilde{A}_S$  and  $\tilde{A}_L$  are proportional to the spin and orbital Hall angles ( $\gamma_{\rm SH}$  and  $\gamma_{\rm OH}$ ), respectively (see Methods).

Taking W|Ni as an example, the MC-TEM provides excellent fits across the full measured thickness range ( $d_W$ = 0 - 15 nm), capturing both amplitude (see Fig. 2c) and waveform evolution. Typical fitting results are shown in Figs. 4a1-a6, with additional results shown in SM Section S8. In particular, the model accurately reproduces non-monotonic intensity trend (Fig. 4b). Figure 4c presents the extracted amplitudes  $A_L$ ,  $A_S$ , and  $A_{Ni}$  as a function of  $d_W$ . The fitting results confirmed our early qualitative analysis that the terahertz intensity minimum is caused by the destructive interference between the spin and orbital contributions ( $A_S$ + $A_L$  $\approx$ 0).

In our model, the diffusion lengths manifest in the short- $d_W$  regime as the initial rise of terahertz amplitude: a sharper rise corresponds to a shorter diffusion length, following the relation of  $\tanh(d_W/2\lambda_m)^{-37}$ , with  $\lambda_m$  being the spin ( $\lambda_s$ ) and effective orbital ( $\lambda_L^{\text{eff}}$ ) diffusion lengths (Fig. 4c). At larger  $d_W$ , the amplitude decrease is governed by optical absorption and electrical shunting effects (see Methods). We note

that this model is fundamentally different from previous analysis based on orbital-current transport to the SiO<sub>2</sub>|W interface<sup>18</sup>. For W|Ni, we extract a significantly shorter orbital diffusion length ( $\lambda_L^{\rm eff} \approx 0.36$  nm) compared to spin ( $\lambda_S \approx 2.20$  nm), consistent with our qualitative analysis.

The MC-TEM fitting also qualitatively reproduces the anomalous behaviors and phase shifts observed in Ni|W, which consistently yields an ultrashort effective orbital diffusion length ( $\lambda_L^{\rm eff} \approx 0.35$  nm; see the SM Section S10).

We extend our high-resolution measurements to the Ta|Ni and Pt|Ni heterostructures and their respective Fe-based counterparts. The two-dimension waveform plots are shown in Figs. 5c-f, with the corresponding terahertz amplitudes extracted at t=0 plotted in Figs. 5a-b.

In Ta|Ni, the terahertz signal exhibits a polarity opposite to that observed in Ta|Fe (Figs. 5c-d), but aligns with the polarity of Pt|Fe (Fig. 5f). This behavior is inconsistent with the ISHE given that Ta and Pt have opposite spin Hall angles<sup>9,20,32</sup>, suggesting the dominant orbital contribution in Ta|Ni, consistent with recent studies<sup>20</sup>. Moreover, our high-resolution measurements show that the terahertz amplitude rises more sharply and peaks at a smaller  $d_W$  in Ta|Ni compared to Ta|Fe (Fig, 5a), suggesting a shorter orbital diffusion length. In the Pt|Ni system, no polarity reversal occurs (Figs. 5e-f), as Pt possesses spin and orbital Hall angles of the same sign<sup>9,31,32</sup>. Nonetheless, the terahertz amplitude in Pt|Ni still peaks at a shorter  $d_W$  compared to Pt|Fe (Fig. 5b), again indicating a shorter characteristic diffusion length when orbital contributions are involved.

The MC-TEM provides excellent fits to both amplitude and waveform data across these systems (see SM Section S8), with the extracted fitting parameters summarized in Table 1. To account for potential amplitude fluctuations between measurements, the spin and orbital amplitude coefficients ( $\tilde{A}_S$  and  $\tilde{A}_L$ ) are normalized to the Ni-layer emission amplitude (b; see Methods). It is important to note that the MC-TEM is constrained not only by amplitude vs. thickness trends, but also by the full terahertz waveform at each thickness. This high-dimensional data space makes the parameter extraction highly constrained, significantly reducing fitting ambiguity. Error landscapes and fitting robustness are discussed in SM Section S9.

Finally, Fig. 5g summarizes the extracted spin and orbital amplitude coefficients  $(\tilde{A}_S/b)$  and  $(\tilde{A}_L/b)$  across all three HM|Ni systems. The signs of the amplitudes are consistent with the first-principles predictions for those of the intrinsic spin and orbital Hall conductivities ( $\sigma_{SH}$  and  $\sigma_{OH}$ ) of each HM (Fig. 5h)<sup>9,20,32</sup>, providing further validation of our model. Notably, the theoretical calculations show that the signs of  $\sigma_{SH}$  and  $\sigma_{OH}$  remain unchanged within an energy window extending up to ~1 eV above the Fermi level <sup>9,20,32</sup> – the relevant range for our optical excitation – reinforcing the robustness of this agreement between experiment and theory.

While recent theoretical studies propose that extrinsic mechanisms could play an important role to the orbital Hall effect, particularly in disordered or engineered systems such as graphene, transition metal dichalcogenides, and topological materials<sup>50–52</sup>, our experimental results show agreement on the relative signs of the *intrinsic*  $\sigma_{SH}$  and  $\sigma_{OH}$  predicted for bulk heavy metals (Fig. 5g-h). This strongly suggests that, in our case, the

observed spin and orbital transport behaviors are primarily governed by intrinsic properties rather than extrinsic contributions.

## **Discussion**

The fitting-derived parameters are summarized in Table 1. A key finding is that orbital currents exhibit consistently shorter effective diffusion lengths than their spin counterparts ( $\lambda_L^{\rm eff} < \lambda_S$ ) across all three HM materials (W, Ta, and Pt). In particular, the effective orbital diffusion length in W is remarkably short ( $\lambda_L^{\rm eff} \approx 0.36$  nm), corresponding to the scale of a single unit cell. For Ta and Pt,  $\lambda_L^{\rm eff}$  is 0.84 and 0.94 nm, respectively, spanning several unit cells.

The intriguing anomalous emission behaviors observed in HM|Ni heterostructures in the ultrathin regime ( $d_{\rm HM}$ <3 nm) is essential for revealing the important orbital contributions, in particular the pronounced non-monotonic behavior in W|Ni. However, given the sensitivity of ferromagnetic Ni to adjacent layers, a key question is whether the observed features could instead arise from the variations in the internal spin-to-charge conversion processes in Ni, affected by proximity to the W layer.

Indeed, recent spin-torque ferromagnetic resonance studies have shown that self-induced spin-orbit torques in the FM layer could affect the experimental interpretation with characteristics that resemble those attributed to orbital transport<sup>53</sup>. In addition, the AHE in Ni could also be enhanced by either imbalanced spin-current reflections at the HM|FM interfaces<sup>42,43</sup>, or from the generation of a longitudinal temperature gradient<sup>54,55</sup>.

However, these possible contributions can be effectively ruled out by our spacer-

layer insertion control experiments. As shown in Fig. 3c (and also see SM Section S5), the insertion of 1-nm Cu, 2-nm Cu, or 1-nm Al at the W|Ni interface does not suppress the terahertz amplitude peak around  $d_W\approx0.8$  nm, nor does it significantly shift its position. Considering these spacer layers effectively disrupt the coupling between the W and the Ni layers, if the observed peak originated from internal processes within Ni modulated by the adjacent W layer, spacer insertion would be expected to eliminate or strongly perturb the effect. The consistent presence and position of the amplitude peak across all configurations clearly demonstrates that the anomalous behavior is intrinsically associated with the W layer, rather than arising from internal spin-to-charge conversion processes within Ni.

To further isolate potential contributions from internal spin-to-charge conversion in FMs, we performed additional control experiments on Cu|Fe heterostructures. Here, Fe was selected to avoid orbital-related conversion processes, and Cu, with its weak spin-orbit coupling, was chosen to minimize the ISHE contributions. If the non-monotonic trend in W|Ni were driven by Ni-based spin-to-charge conversion modulated by adjacent metals, a similar trend should appear in Cu|Fe. However, as shown in the SM Fig. S24, the terahertz emission from Cu|Fe decreases monotonically with increasing Cu thickness, unlike the pronounced peak observed in W|Ni. This contrast further supports the conclusion that the ultrathin-regime anomalies in W|Ni are not due to internal FM-layer mechanisms.

While our study offers new insights into the ultrashort orbital diffusion lengths observed in HMs, the understanding of orbital transport remains in its early stage, with

several important aspects requiring further investigation.

First, recent theoretical studies<sup>25,49</sup> have proposed that orbital-to-spin interconversion can occur in materials with strong spin-orbit coupling. The resulting spin currents could consequently be converted into transverse charge currents via ISHE, leading to terahertz emission. Our MC-TEM model does not explicitly distinguish this two-step process, but only considers the net effect with the effective orbital diffusion length ( $\lambda_L^{\text{eff}}$ ). Since the extracted  $\lambda_L^{\text{eff}}$  is already significantly shorter than  $\lambda_S$  in HMs, this implies that if the two-step process was explicitly taken into account, the actual orbital diffusion length could be even shorter than the reported values in Table 1. Notably, in the cases of Ta and Pt, the observation that  $\lambda_L^{\text{eff}}$  is comparable to  $\lambda_S$  may suggest that a portion of the detected orbital-related signals may originate from this two-step conversion process <sup>23,25</sup>. Disentangling this secondary process will require further experimental and theoretical studies, particularly in materials with weak spin-orbit coupling or negative orbital Hall angles.

Second, the extracted spin and orbital diffusion lengths are shorter than the conventional spin-flipped diffusion length measured under steady-state spin transport<sup>56,57</sup>. This observation is not unique to our work. Similar few-nanometer spin diffusion lengths have been widely reported in prior terahertz emission spectroscopy studies<sup>37,38,47</sup>. The shorter apparent diffusion lengths likely arise from the hot-electron nature of the laser-induced terahertz emission process, as recently supported by superdiffusive spin transport simulations<sup>58</sup>. Whether the key conclusion – that orbital diffusion lengths are shorter than spin diffusion lengths in HMs – can extend to spin

and orbital transport near the Fermi level, as probed in spin-pumping or steady-state spintronic experiments, remains an open question. Addressing this issue will require future studies using complementary experimental techniques.

Finally, the CEP offset,  $\Delta \varphi$ , is essential for accurately reproducing the experimental terahertz waveforms. This is particularly evident for the W|Ni samples with  $d_W$ =2-3 nm, where the spin and orbital contributions nearly cancel (Figs. 4a3-a4). However, for the Ni|W data, the MC-TEM with a thickness-independent  $\Delta \varphi$  yields only a qualitative agreement with the experiment trends and deviate from the detailed amplitudes and waveforms (see SM Section S10). These findings indicate that the phase offsets may be affected by extrinsic effects such as interface quality or growth conditions, which warrant further systematic studies.

In conclusion, we employ a wedge-shaped sample platform combined with terahertz emission spectroscopy to systematically investigate spin and orbital transport in HM|Ni heterostructures. Our high-resolution measurements access the previously unexplored ultrathin film regime ( $d_{\rm HM}$ < 3 nm), revealing anomalous behaviors that challenge prevailing interpretations of long-range orbital transport. These findings underscore the critical importance of the wedge-sample approach, which enables continuous, sub-nanometer thickness scanning – essential for resolving subtle waveform variations and disentangling competing emission mechanisms. While our results demonstrate that orbital transport in HMs is highly localized, previous reports of long orbital diffusion lengths in light metals such as Ti, Cr, and Cu<sup>11,20,29</sup> suggest a potential material-dependent behavior that warrants further investigation.

#### Methods

Sample preparation and characterization. Wedge-shaped HM|FM heterostructures were fabricated on double-side-polished Al<sub>2</sub>O<sub>3</sub>(0001) substrates. Prior to deposition, all substrates were annealed at 150°C for one hour in the sputtering chamber with a base pressure of 2×10<sup>-8</sup> torr. A 4-nm SiO<sub>2</sub> buffer layer was first deposited onto the substrate. The HM|FM heterostructure was then deposit via DC magnetron sputtering at room temperature under an argon pressure of 3 mTorr. Finally, a 4-nm SiO<sub>2</sub> capping layers was deposited to prevent sample oxidation. The pre-deposition of a SiO<sub>2</sub> buffer layer ensures that the FM|HM heterostructure is encapsulated between SiO<sub>2</sub> layers. Al<sub>2</sub>O<sub>3</sub>(0001) was selected as the substrate material for its high thermal conductivity, which helps mitigate the laser-induced heating and potential sample damage during measurements.

Prior to deposition, the deposition rates of W, Ta, and Pt were systematically calibrated using X-ray reflectometry. To precisely control the HM-layer thickness, wedge-shaped profiles were fabricated by controlling the deposition time during sputtering using a mechanical shutter. The shutter was moved in front of the sample surface at a constant, calibrated velocity, producing a continuous thickness gradient along x in the HM layer, over a lateral distance of 1.0 cm. In this study, the HM-layer thickness gradients were 1.60 nm/mm for W, 2.50 nm/mm for Ta, and 1.33 nm/mm for Pt.

Post-deposition, the spatial variation in the HM-layer thickness along the *x*-axis was validated by measuring the transmission of a near-infrared femtosecond laser beam,

confirming the expected thickness gradient (see SM Section S1).

**Experimental setup.** Terahertz radiation was generated using a power-stabilized fiber oscillator (FIBRE SP, Nanjing Keyun Optoelectronics Ltd.), delivering laser pulses with a duration of 110 fs, a repetition rate of 36 MHz, a central wavelength of 1030 nm, and a maximum power of 3.3 W. In our experiments, a typical excitation power of  $\sim$ 0.7 W was used, with the beam incident from the substrate-side of the samples. An external magnetic field (H) of 1000 Oe was applied along the x-axis to saturate the magnetization of the FM layer.

The emitted terahertz waves were collected and focused by a pair of off-axis parabolic mirrors. The  $E_y$  component was selected by a terahertz polarizer, and was subsequently measured using the electro-optic sampling. A 1-mm-thick GaP was used as the detection crystal. To isolate the H-dependent signals and exclude potential signals from electrical anisotropy<sup>47</sup>, we recorded the differential response by subtracting the signals measured under opposite magnetic-field directions (+x and -x).

To investigate the HM-thickness-dependent terahertz emission, the sample was translated laterally along the *x*-axis with a step size of 0.1 mm, enabling spatial mapping across the HM wedge. The excitation beam was focused to a radius of 50  $\mu$ m. Given the HM-layer thickness gradient of ~1.6 nm/mm, this configuration yields a thickness resolution of ~0.16 nm.

Multi-component terahertz emission model. In the frequency domain, the terahertz electric field  $\tilde{\mathbf{E}}(\omega)$  is governed by the inhomogeneous wave equation<sup>59</sup>:

$$-\nabla \times (\nabla \times \tilde{\mathbf{E}}) + \frac{n^2 \omega^2}{c^2} \tilde{\mathbf{E}} = -\frac{i Z_0 \omega}{c} \tilde{\mathbf{J}}, \tag{3}$$

where '~' denotes the frequency-domain quantities, n is the refractive index,  $\omega/2\pi$  is the terahertz frequency, c is the vacuum speed of light, and  $Z_0$  is the vacuum impedance. The total current density  $\tilde{J}$  comprises four primary contributions:

(1) ISHE, 
$$\tilde{\mathbf{j}}_{\text{ISHE}} = \gamma_{\text{SH}} \tilde{\mathbf{j}}_{S} \times \mathbf{M}/|\mathbf{M}|$$
,

(2) IOHE, 
$$\tilde{\mathbf{j}}_{IOHE} = \gamma_{OH}\tilde{\mathbf{j}}_L \times \mathbf{M}/|\mathbf{M}|$$
,

(3) AHE, 
$$\tilde{\mathbf{j}}_{AHE} = \gamma_{AHE} \tilde{\mathbf{j}}_S \times \mathbf{M}/|\mathbf{M}|$$
,

(4) MDE, 
$$\tilde{\mathbf{j}}_{\text{MDE}} = (\partial_z \tilde{M}) \hat{y}$$
,

where  $\tilde{\mathbf{J}}_S$  and  $\tilde{\mathbf{J}}_L$  are the spin and orbital currents injected along the z-axis,  $\mathbf{M}$  is the FM magnetization (aligned along x), and  $\hat{\mathbf{y}}$  is the unit vector in the x-direction. Under these conditions, all transverse current components ( $\tilde{\mathbf{J}}_{ISHE}$ ,  $\tilde{\mathbf{J}}_{IOHE}$ ,  $\tilde{\mathbf{J}}_{AHE}$ , and  $\tilde{\mathbf{J}}_{MDE}$ ) are polarized along the y-axis.

The corresponding terahertz electric field  $\tilde{E}(\omega)$ , immediately behind the sample, can be calculated by the *z*-integration of the transverse charge current densities<sup>37</sup>:

 $\tilde{E}(\omega) = eZ_{\rm eff} \left\{ \int_0^{d_{\rm HM}} [\gamma_{\rm SH} \tilde{\jmath}_S(\omega, z) + \gamma_{\rm OH} \tilde{\jmath}_L(\omega, z)] dz + \int_{-d_{\rm FM}}^0 [\gamma_{\rm AHE} \tilde{\jmath}_S(\omega, z) + \partial_z \tilde{M}(\omega)] dz \right\},$  (4) where  $Z_{\rm eff}$  is the effective impedance, given by  $Z_{\rm eff} = \frac{Z_0}{n_1 + n_2 + Z_0 \cdot (\sigma_{\rm FM} \cdot d_{\rm FM} + \sigma_{\rm HM} \cdot d_{\rm HM})},$  with  $Z_0 = 377~\Omega$  being vacuum impedance<sup>37</sup>. Here, we assume that the refractive indices of the substract  $(n_1)$  and air  $(n_2)$ , and the conductivities  $(\sigma_{\rm FM}$  and  $\sigma_{\rm HM})$  are dispersionless within the relevant terahertz frequency range.

We then perform Fourier transform to obtain the time-domain terahertz field amplitudes  $\tilde{E}(\omega) \to E(t)$ , and evaluate the individual contributions from each mechanism. Since the FM-layer thickness  $d_{\rm FM}$  is fixed and the HM-layer thickness  $d_{\rm HM}$  is varied, the time-domain field amplitudes can be written as:

$$\begin{cases} E_{S}(t, d_{\text{HM}}) = eZ_{\text{eff}}(d_{\text{HM}}) \int_{0}^{d_{\text{HM}}} \gamma_{\text{SH}} j_{S}(t, z) dz \\ E_{L}(t, d_{\text{HM}}) = eZ_{\text{eff}}(d_{\text{HM}}) \int_{0}^{d_{\text{HM}}} \gamma_{\text{OH}} j_{L}(t, z) dz \\ E_{\text{Ni}}(t, d_{\text{HM}}) = eZ_{\text{eff}}(d_{\text{HM}}) \int_{-d_{\text{Ni}}}^{0} [\gamma_{\text{AHE}} j_{S}(t, z) + \partial_{z} M(t, z)] dz \end{cases}$$
 (5)

The total time-domain electric field is then given by  $E(t, d_{\rm HM}) = E_S(t, d_{\rm HM}) + E_L(t, d_{\rm HM}) + E_{\rm Ni}(t, d_{\rm HM})$ .

This model can be further simplified based on several key experimental observations. First, the ISHE waveform  $E_S(t)$  is found to be effectively invariant with respect to  $d_{HM}$ , as confirmed by measurements on the HM|Fe and Fe|HM samples (see Figs. 2f and h, and Figs. 5d and f). Second, while the introduction of a W|Ni interface could potentially alter the  $E_{Ni}(t)$  waveform, our high-resolution data show that the waveform remains unchanged for ultrathin W layers ( $d_W$ <0.5 nm), where the ISHE and IOHE contributions are negligible (see SM Fig. S7). This allows us to assume the  $E_{Ni}(t)$  waveform also independent of  $d_{HM}$ . Third, although the microscopic understanding of orbital transport remains less well understood, our experimental results, particularly those from Ta|Ni (Fig. 5c), indicate that the IOHE waveforms are largely unaffected by variations in  $d_{HM}$ , justifying a similar assumption for  $E_L(t)$ .

Under these considerations, each terahertz-signal component can be factorized into a thickness-dependent amplitude  $A_m(d_{\rm HM})$  and a thickness-independent temporal waveform  $\mathcal{E}_m(t)$ , such that:  $E_m(t,d_{\rm HM})=A_m(d_{\rm HM})\cdot\mathcal{E}_m(t)$ , with m=S,L, Ni. This decomposition leads directly to Eq. (1) in the main text.

Considering the effects of optical absorption, interfacial reflections of spin and orbital currents, and the electrical shunting from adjacent layers, we obtain<sup>37</sup>:

$$A_{S(L)}(d_{\mathrm{HM}}) = \lambda_{S(L)}^{(\mathrm{eff})} \frac{\gamma_{\mathrm{SH(OH)}} \cdot a_{S(L)}}{d_{\mathrm{HM}} + d_{\mathrm{FM}}} \frac{\tanh(d_{\mathrm{HM}}/2\lambda_{S(L)}^{(\mathrm{eff})})}{n_1 + n_2 + Z_0 \cdot (\sigma_{\mathrm{FM}} \cdot d_{\mathrm{FM}} + \sigma_{\mathrm{HM}} \cdot d_{\mathrm{HM}})}, \tag{6}$$

where  $a_{S(L)}$  is the injected spin or orbital current density,  $n_1$  and  $n_2$  are the substrate/air refractive indices, and  $\sigma_{FM}$  and  $\sigma_{HM}$  are the terahertz conductivities of the FM and HM layers, respectively. Here, both the spin and orbital channels are modeled under the same formalism.

For the Ni-layer contribution, since the Ni layer thickness ( $d_{Ni}$ ) is fixed, the transverse terahertz current density in Ni can be treated as a constant current source. Considering the optical absorption and shunting effects, its amplitude exhibits a monotonic decrease with increasing  $d_{HM}$ , and is given by:

$$A_{\text{Ni}}(d_{\text{HM}}) = \frac{b \cdot d_{\text{Ni}}}{d_{\text{HM}} + d_{\text{Ni}}} \frac{1}{n_1 + n_2 + Z_0 \cdot (\sigma_{\text{Ni}} \cdot d_{\text{Ni}} + \sigma_{\text{HM}} \cdot d_{\text{HM}})},\tag{7}$$

where b is a coefficient proportional to Ni-layer emission amplitude.

The temporal waveforms  $\mathcal{E}_m(t)$  are directly determined using experimental measurements. The waveform  $\mathcal{E}_{Ni}(t)$  is directly extracted from the terahertz emission from a 5-nm Ni film and normalized to its peak amplitude (see SM Section S3). For the spin and orbital waveforms,  $\mathcal{E}_S(t)$  and  $\mathcal{E}_L(t)$ , we first analyze the terahertz spectra and phases of three representative samples: W(0.8)|Ni, W(6.6)|Ni, and W(0.8)|Fe (see SM Fig. S23). According to our earlier analysis, the emission from W(0.8)|Ni is predominantly orbital in nature, while W(6.6)|Ni and W(0.8)|Fe are both spin-dominant. Notably, all three samples exhibit nearly identical terahertz spectra. In particular, the spectral and phase agreement between W(6.6)|Ni and W(0.8)|Fe further supports our conclusion that ISHE dominates the emission from W|Ni when  $d_W>3.0$  nm.

Given the nearly identical terahertz spectra across these samples, we adopt the

experimentally measured waveform from the HM|Fe heterostructures, denoted  $\tilde{\mathcal{E}}_{S,\text{expt}}(t)$ , as the spin-component waveform:

$$\mathcal{E}_{S}(t) = \tilde{\mathcal{E}}_{S,\text{expt}}(t). \tag{8}$$

The orbital waveform is modeled by applying a CEP shift  $\Delta \varphi$  to the spin waveform, which leads to Eq. (2).

Substituting Eqs. (2 and 6-8) into Eq. (1) yields the MC-TEM, which we use to extract key parameters associated with spin and orbital contributions. Most variables, such as  $n_1$ ,  $n_2$ ,  $\sigma_{\text{FM}}$ ,  $\sigma_{\text{HM}}$ ,  $\lambda_S$ , and b, can be determined either by reference databases or by direct measurements (see Methods and SM Section S4). Consequently, for each HM|Ni sample, only 4 independent fitting parameters remain: the effective orbital diffusion length in HM ( $\lambda_L^{\text{eff}}$ ), the ISHE/IOHE amplitude coefficients ( $\tilde{A}_S = \gamma_{\text{SH}} \cdot a_S$ ,  $\tilde{A}_L = \gamma_{\text{OH}} \cdot a_L$ ) and the CEP offset ( $\Delta \varphi$ ).

Parameter determination and fitting procedure. In the MC-TEM, several key parameters are determined prior to fitting. First, the refractive index of air is fixed at  $n_2$ =1, while the refractive index of the substrate  $n_1$  and the terahertz conductivities  $\sigma_{\text{FM}}$  and  $\sigma_{\text{HM}}$  are experimentally determined via terahertz transmission spectroscopy. Detailed experimental results are shown in SM Section S4. Second, the spin diffusion length  $\lambda_{\text{S}}$  in HM is independently extracted by fitting the terahertz amplitude from HM|Fe heterostructures as a function of  $d_{\text{HM}}$ , using the MC-TEM by setting  $A_L$ =0 and  $A_{\text{Ni}}$ =0<sup>37</sup>. The fitting results for W|Fe, Ta|Fe, and Pt|Fe are shown in Figs. 2c, and 5a-b, respectively. Finally, the amplitude coefficient b associated with the AHE+MDE contribution in Ni is determined from the terahertz signal of the HM|Ni wedge-shaped

sample evaluated at  $d_{\text{HM}}$ =0, where the signal originates solely from the Ni layer. The above parameter values are provided in SM Table S2.

With these parameters determined, we have 4 independent fitting variables remain for each HM|Ni sample:  $\lambda_L^{\text{eff}}$ ,  $\tilde{A}_S$ ,  $\tilde{A}_L$ , and  $\Delta \varphi$ . These parameters are subsequently extracted by performing a global fitting procedure using a genetic algorithm to minimize the deviation between the modeled and experimental terahertz waveforms at different  $d_{\text{HM}}$ . In SM Section S9, we provide a detailed discussion on the fitting robustness and error landscapes, which yields the error bars presented in Table 1.

Table 1. Key parameters extracted using the MC-TEM for different HMs.

	W	Ta	Pt
$\lambda_{S}$ (nm)	2.20±0.13	$1.34 \pm 0.07$	2.00±0.34
$\lambda_L^{ m eff}({ m nm})$	0.36±0.17	$0.84 \pm 0.51$	0.94±0.44
$\tilde{A}_S/b$ (arb. units)	-50.4±9.0	-18.2±14.7	25.0±20.9
$\tilde{A}_L/b$ (arb. units)	162.9±25.5	$107.9\pm28.4$	133.4±42.6
$\Delta \varphi$ (rad)	0.016±0.080	$0.012\pm0.147$	-0.045±0.075

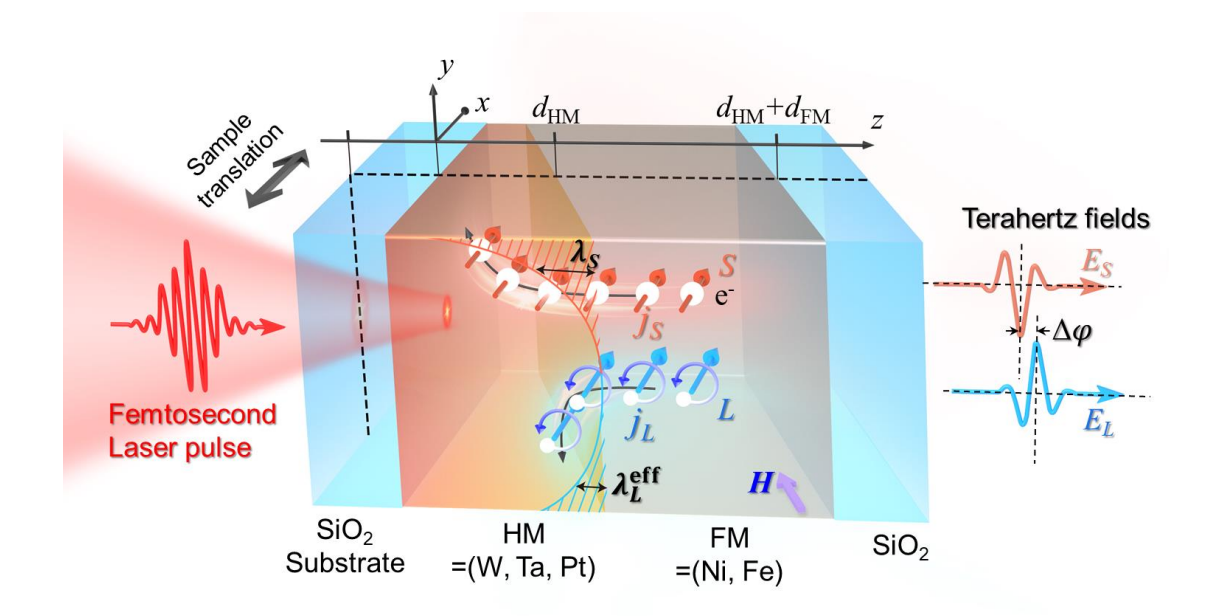


Figure 1. Schematic Illustration of the Experimental Principle. Femtosecond laser excitations launches S and L propagation from the FM layer into the adjacent HM layer, leading to spin  $(j_S)$  and orbital  $(j_L)$  currents. These currents are subsequently converted into transverse charge currents via the ISHE and IOHE, producing terahertz fields  $E_S$  and  $E_L$ , respectively. The HM layer is fabricated with a wedge-shaped thickness gradient along the x direction, enabling continuous variation of HM thickness by scanning the sample position. For illustrative purpose, the figure depicts the transverse charge currents from  $j_S$  and  $j_L$  as flowing in opposite directions. In reality, their relative directions vary: they are opposite in W and Ta, but are aligned in Pt.

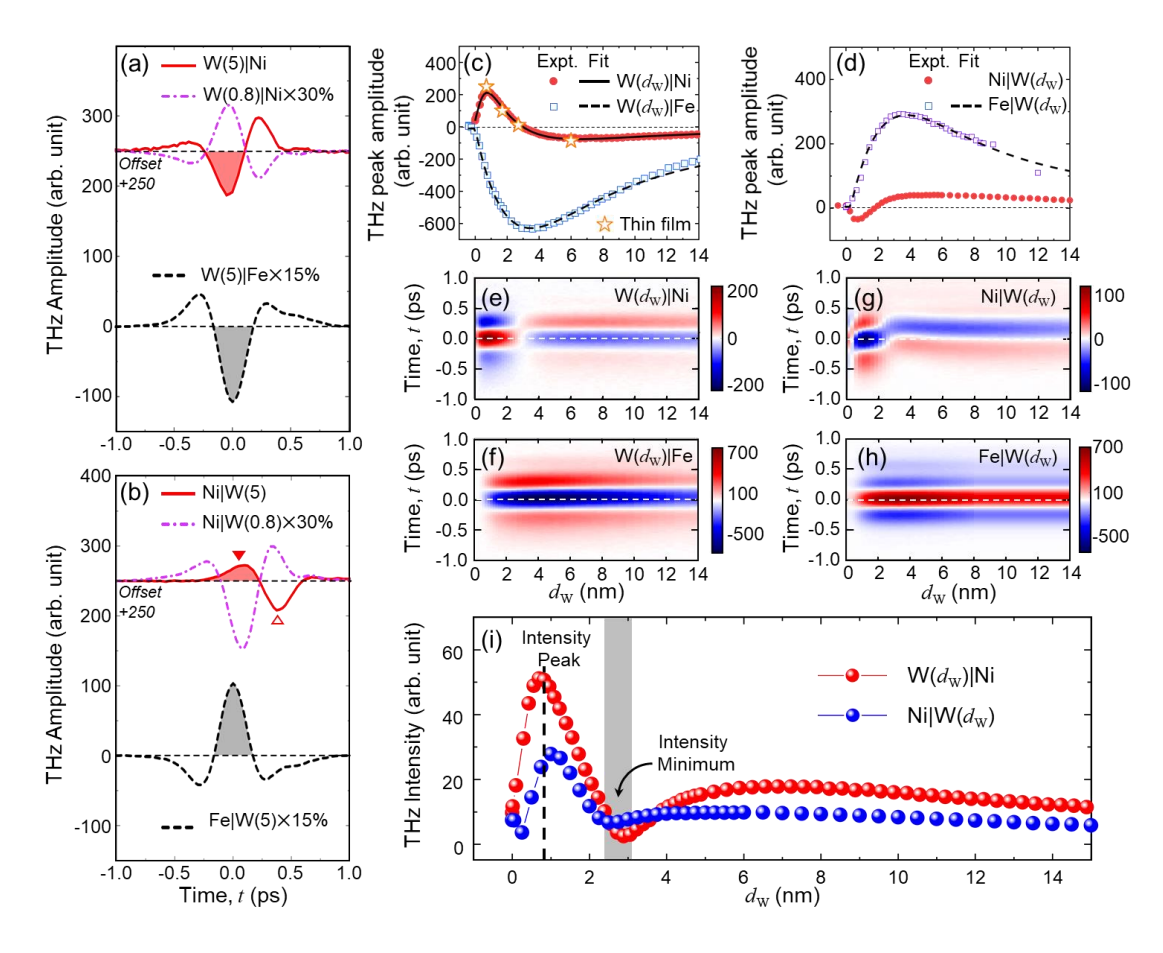


Figure 2. Terahertz Emission from W|Ni and Ni|W. a. Representative terahertz waveforms from W(5)|Ni, W(0.8)|Ni, and W(5)|Fe. For clarity, W|Ni waveforms are vertically offset by +250, and the amplitudes of W(0.8)|Ni and W(5)|Fe are scaled by 30% and 15%, respectively. Signal polarities at t=0 for W(5)|Ni and W(5)|Fe are indicated. b. Same as a., but for Ni|W and Fe|W heterostructures. The positive peak at t=0 and the negative peak at  $t\approx0.3$  ps of Ni|W(5) are respectively indicated. c. Terahertz amplitudes extracted at t=0 for W|Ni and W|Fe. Symbols represent experimental data; solid and dashed lines indicate fits based on the MC-TEM. Star symbols denote measurements from discrete thin-film samples. d. Same as c., but for Ni|W and Fe|W. e.-h. Two-dimensional waveform plots as a function of  $d_W$  for W|Ni (e), W|Fe (f), Ni|W (g), and Fe|W (h). i. Spectral intensities of W|Ni and Ni|W as a function of  $d_W$ . Common intensity peaks near  $d_W\approx0.8$  nm and minimums around 2.8 nm are highlighted.

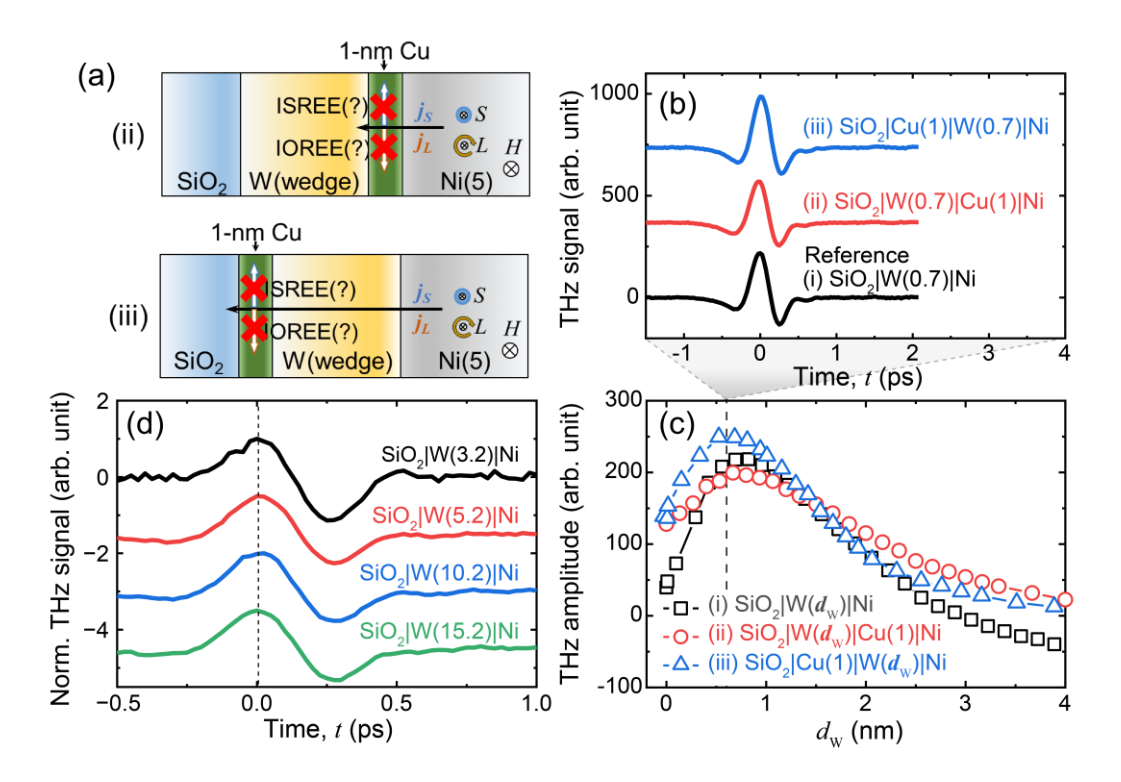


Figure 3. Control Experiments Excluding Interfacial Conversion Mechanisms. a.

Schematic illustrations of configurations with 1-nm Cu spacer layers inserted at different interfaces: configuration (ii) with Cu at the W|Ni interface, and configuration (iii) with Cu at the SiO<sub>2</sub>|W interface. Cu insertion is designed to disrupt interfacial conversion processes such as the ISREE and IOREE. b. Experimental terahertz waveforms from three sample configurations: (i)  $SiO_2|W(0.7)|Ni$ , (ii)  $SiO_2|W(0.7)|Cu(1)|Ni$ , and (iii)  $SiO_2|Cu(1)|W(0.7)|Ni$ . c. Terahertz amplitudes extracted at t=0 as a function of  $d_{\rm W}$  from all three configurations, showing consistent peak behavior near  $d_{\rm W} \approx 0.7$ -0.8 nm. **d.** Normalized terahertz waveforms from  $SiO_2|W|Ni$  heterostructures with varying  $d_W$ . Peak positions are denoted by a dashed line.

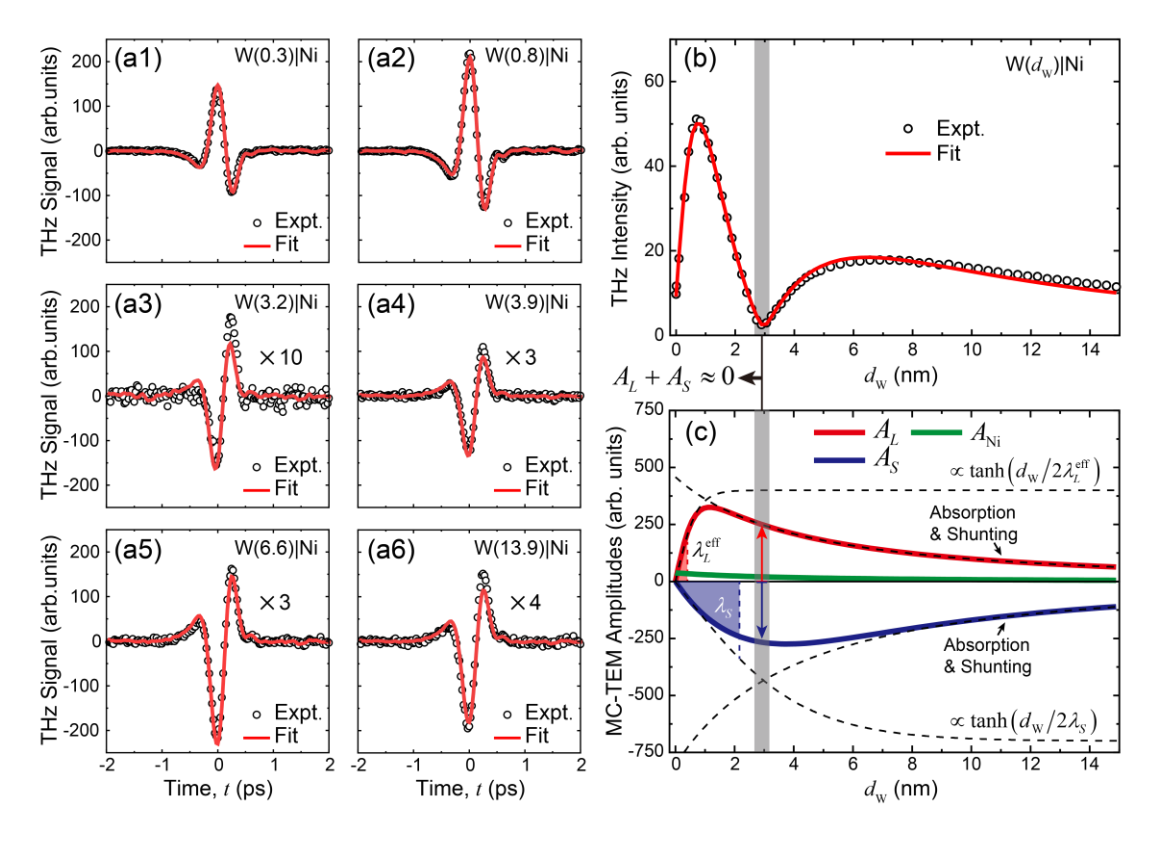


Figure 4. Model Fitting of Terahertz Emission Using MC-TEM. a1-a6.

Representative fits to the time-domain terahertz waveforms from W|Ni samples with varying W-layer thickness ( $d_W$ ) based on MC-TEM. Symbols represent experimental data; solid lines indicate model fits. **b.** Spectrally integrated terahertz intensity from W( $d_W$ )|Ni as a function of  $d_W$ . Experimental data (symbols) are well captured by the model fits (solid line). **c.** Extracted amplitudes  $A_L$ ,  $A_S$ , and  $A_{Ni}$  as a function of  $d_W$ . The effective orbital ( $\lambda_L^{eff}$ ) and spin ( $\lambda_S$ ) diffusion lengths are indicated. Signal rising associated with spin- and orbital bulk conversion processes, and the decay due to optical absorption and shunting effects are presented as dashed lines for illustrative purposes. The intensity minimum in **c.** corresponds to the W thickness where destructive interference occurs between spin and orbital contributions, i.e.,  $A_L + A_S \approx 0$ .

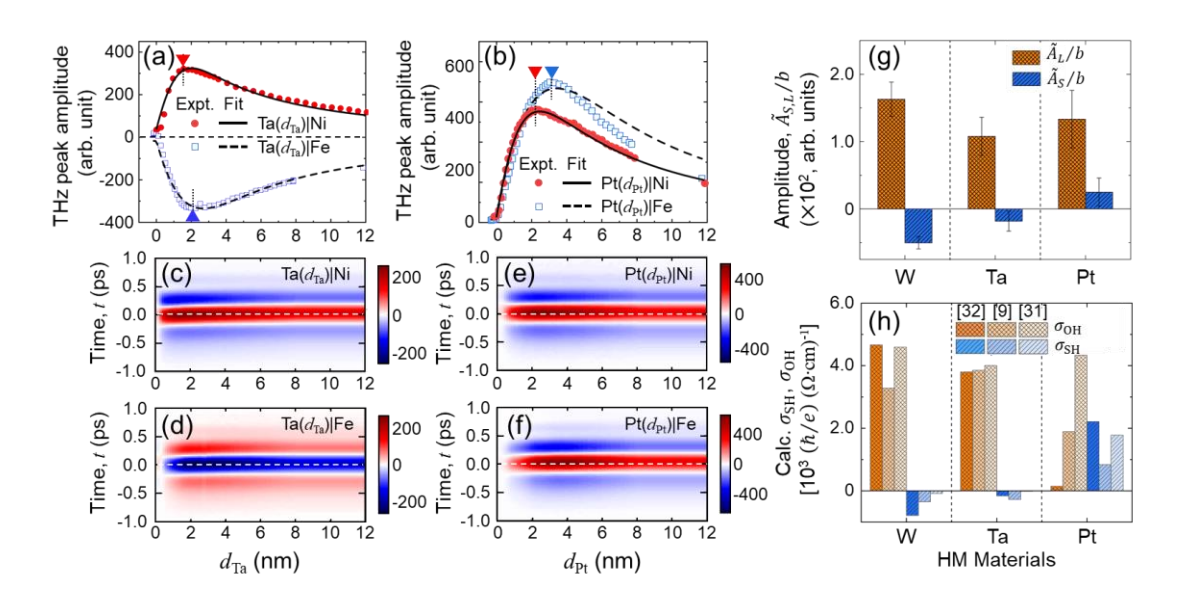


Figure 5. Distinguishing Spin and Orbital Contributions. a. Terahertz amplitudes extracted at t=0 for Ta|Ni and Ta|Fe. Symbols represent experimental data; solid and dashed lines indicate fits based on the MC-TEM. Peak positions are highlighted by triangle symbols. b. Same as a., but for Pt|Ni and Pt|Fe. c.-f. Two-dimensional waveform plots as a function of  $d_W$  for Ta|Ni (c), Ta|Fe (d), Pt|Ni (e), and Pt|Fe (f). g. Normalized amplitude coefficients  $\tilde{A}_S/b$  (spin) and  $\tilde{A}_L/b$  (orbital) as a function of different HM materials, obtained by fitting experimental data using the MC-TEM. h. Ab-initio calculated values of the spin ( $\sigma_{SH}$ ) and orbital Hall ( $\sigma_{OH}$ ) conductivities for the corresponding HM materials  $^{9,31,32}$ .

Acknowledgments: This work was accomplished in Fudan University. We acknowledge the support from the National Key Research and Development Program of China (Grant Nos. 2024FYA1408500, 2021YFA1400200, and 2022YFA1404700). We also acknowledge the support from the National Natural Science Foundation of China (Grant Nos. 12450407, 12274091, 12434003, and 12274083), and the support from the Shanghai Municipal Science and Technology (Grant No. 22JC1400200).

Inclusion & ethics statement: All collaborators of this study have fulfilled the criteria for authorship required by Nature Portfolio journals have been included as authors, as their participation was essential for the design and implementation of the study. Roles and responsibilities were agreed among collaborators ahead of the research. This work includes findings that are locally relevant, which have been determined in collaboration with local partners. This research was not severely restricted or prohibited in the setting of the researchers, and does not result in stigmatization, incrimination, discrimination or personal risk to participants. Local and regional research relevant to our study was taken into account in citations.

**Data availability:** The minimum dataset is available in the main text, the supplementary information and the supplementary dataset. Additional data are available upon request to the corresponding author, Y. W. and Z. T.

**Code availability:** Sources code for multi-component terahertz emission model fitting are provided as Supplementary Information. Additional codes are available upon request to the corresponding author, Y. W. and Z. T.

## References

- 1. Go, D. *et al.* Toward surface orbitronics: Giant orbital magnetism from the orbital Rashba effect at the surface of spmetals. *Sci. Rep.* **7**, 46742 (2017).
- 2. Phong, V. T. *et al.* Optically Controlled Orbitronics on a Triangular Lattice. *Phys. Rev. Lett.* **123**, 236403 (2019).
- 3. Bernevig, B. A., Hughes, T. L. & Zhang, S. C. Orbitronics: The intrinsic orbital current in p-doped silicon. *Phys. Rev. Lett.* **95**, 066601 (2005).
- 4. Go, D., Jo, D., Lee, H. W., Kläui, M. & Mokrousov, Y. Orbitronics: Orbital currents in solids. *EPL* **135**, 37001 (2021).
- 5. Zutic, I., Fabian, J. & Sarma, S. Das. Spintronics: Fundamentals and applications. *Rev. Mod. Phys.* **76**, 323–410 (2004).
- 6. Fert, A. Nobel lecture: Origin, development, and future of spintronics. *Rev. Mod. Phys.* **80**, 1517–1530 (2008).
- 7. Sinova, J., Valenzuela, S. O., Wunderlich, J., Back, C. H. & Jungwirth, T. Spin Hall effects. *Rev. Mod. Phys.* 87, 1213–1260 (2015).
- 8. Go, D., Jo, D., Kim, C. & Lee, H. W. Intrinsic Spin and Orbital Hall Effects from Orbital Texture. *Phys. Rev. Lett.* **121**, 86602 (2018).
- 9. Kontani, H., Tanaka, T., Hirashima, D. S., Yamada, K. & Inoue, J. Giant orbital hall effect in transition metals: Origin of large spin and anomalous hall effects.

  Phys. Rev. Lett. 102, 016601 (2009).
- 10. Salemi, L., Berritta, M., Nandy, A. K. & Oppeneer, P. M. Orbitally dominated Rashba-Edelstein effect in noncentrosymmetric antiferromagnets. *Nat. Commun.*

- **10**, 5381 (2019).
- 11. Choi, Y. G. *et al.* Observation of the orbital Hall effect in a light metal Ti. *Nature* **619**, 52–56 (2023).
- 12. Ding, S. *et al.* Observation of the Orbital Rashba-Edelstein Magnetoresistance. *Phys. Rev. Lett.* **128**, 67201 (2022).
- Ding, S. et al. Harnessing Orbital-to-Spin Conversion of Interfacial Orbital
   Currents for Efficient Spin-Orbit Torques. Phys. Rev. Lett. 125, 177201 (2020).
- Liao, L. et al. Efficient orbital torque in polycrystalline ferromagnetic-metal/Ru/Al<sub>2</sub>O<sub>3</sub> stacks: Theory and experiment. Phys. Rev. B 105, 104434 (2022).
- Lyalin, I., Alikhah, S., Berritta, M., Oppeneer, P. M. & Kawakami, R. K.
   Magneto-Optical Detection of the Orbital Hall Effect in Chromium. *Phys. Rev. Lett.* 131, 156702 (2023).
- 16. Bose, A. *et al.* Detection of long-range orbital-Hall torques. *Phys. Rev. B* **107**, 134423 (2023).
- 17. Hayashi, H. *et al.* Observation of long-range orbital transport and giant orbital torque. *Commun. Phys.* **6**, 32 (2023).
- Seifert, T. S. et al. Time-domain observation of ballistic orbital-angular-momentum currents with giant relaxation length in tungsten. Nat. Nanotechnol.
   18, 1132–1138 (2023).
- 19. Mishra, S. S., Lourembam, J., Lin, D. J. X. & Singh, R. Active ballistic orbital transport in Ni/Pt heterostructure. *Nat. Commun.* **15**, 4568 (2024).

- 20. Xu, Y. *et al.* Orbitronics: light-induced orbital currents in Ni studied by terahertz emission experiments. *Nat. Commun.* **15**, 2043 (2024).
- 21. Xu, R. *et al.* Terahertz generation via the inverse orbital Rashba-Edelstein effect at the Ni/Cu Ox interface. *Phys. Rev. Res.* **7**, L012042 (2025).
- 22. Go, D. *et al.* Long-Range Orbital Torque by Momentum-Space Hotspots. *Phys. Rev. Lett.* **130**, 246701 (2023).
- 23. Urazhdin, S. Symmetry constraints on orbital transport in solids. *Phys. Rev. B* **108**, L180404 (2023).
- 24. Belashchenko, K. D. *et al.* Breakdown of the drift-diffusion model for transverse spin transport in a disordered Pt film. *Phys. Rev. B* **108**, 144433 (2023).
- 25. Rang, M. & Kelly, P. J. Orbital relaxation length from first-principles scattering calculations. *Phys. Rev. B* **109**, 214427 (2024).
- 26. Zheng, Z. C. *et al.* Magnetization switching driven by current-induced torque from weakly spin-orbit coupled Zr. *Phys. Rev. Res.* **2**, 013127 (2020).
- 27. Boeglin, C. *et al.* Distinguishing the ultrafast dynamics of spin and orbital moments in solids. *Nature* **465**, 458–461 (2010).
- 28. Idrobo, J. C. *et al.* Direct observation of nanometer-scale orbital angular momentum accumulation. *arxiv.org/abs/2403.09269* (2025).
- 29. Lee, S. *et al.* Efficient conversion of orbital Hall current to spin current for spin-orbit torque switching. *Commun. Phys.* **4**, 234 (2021).
- 30. Lee, D. et al. Orbital torque in magnetic bilayers. Nat. Commun. 12, 6710 (2021).
- 31. Salemi, L. & Oppeneer, P. M. First-principles theory of intrinsic spin and orbital

- Hall and Nernst effects in metallic monoatomic crystals. *Phys. Rev. Mater.* **6**, 095001 (2022).
- 32. Go, D., Lee, H. W., Oppeneer, P. M., Blügel, S. & Mokrousov, Y. First-principles calculation of orbital Hall effect by Wannier interpolation: Role of orbital dependence of the anomalous position. *Phys. Rev. B* **109**, 174435 (2024).
- 33. Leitenstorfer, A., Hunsche, S., Shah, J., Nuss, M. C. & Knox, W. H. Detectors and sources for ultrabroadband electro-optic sampling: Experiment and theory. *Appl. Phys. Lett.* **74**, 1516–1518 (1999).
- 34. Wu, Q. & Zhang, X. C. Free-space electro-optic sampling of terahertz beams. *Appl. Phys. Lett.* **67**, 3523 (1995).
- 35. Kampfrath, T. *et al.* Terahertz spin current pulses controlled by magnetic heterostructures. *Nat. Nanotechnol.* **8**, 256–260 (2013).
- 36. Yang, D. *et al.* Powerful and Tunable THz Emitters Based on the Fe/Pt Magnetic Heterostructure. *Adv. Opt. Mater.* **4**, 1944–1949 (2016).
- 37. Seifert, T. *et al.* Efficient metallic spintronic emitters of ultrabroadband terahertz radiation. *Nat. Photonics* **10**, 483–488 (2016).
- 38. Torosyan, G., Keller, S., Scheuer, L., Beigang, R. & Papaioannou, E. T. Optimized Spintronic Terahertz Emitters Based on Epitaxial Grown Fe/Pt Layer Structures. *Sci. Rep.* **8**, 1311 (2018).
- 39. Jungfleisch, M. B. *et al.* Control of Terahertz Emission by Ultrafast Spin-Charge Current Conversion at Rashba Interfaces. *Phys. Rev. Lett.* **120**, 207207 (2018).
- 40. Zhou, C. et al. Broadband Terahertz Generation via the Interface Inverse

- Rashba-Edelstein Effect. Phys. Rev. Lett. 121, 086801 (2018).
- 41. Ni, L. *et al.* Strong interface-induced spin-charge conversion in YIG/Cr heterostructures. *Appl. Phys. Lett.* **117**, 112402 (2020).
- 42. Zhang, Q. *et al.* Terahertz Emission from Anomalous Hall Effect in a Single-Layer Ferromagnet. *Phys. Rev. Appl.* **12**, 054027 (2019).
- 43. Mottamchetty, V. *et al.* Direct evidence of terahertz emission arising from anomalous Hall effect. *Sci. Rep.* **13**, 5988 (2023).
- 44. Liu, Y. *et al.* Separation of emission mechanisms in spintronic terahertz emitters. *Phys. Rev. B* **104**, 064419 (2021).
- 45. Beaurepaire, E. *et al.* Coherent terahertz emission from ferromagnetic films excited by femtosecond laser pulses. *Appl. Phys. Lett.* **84**, 3465–3467 (2004).
- 46. Zhang, W. et al. Ultrafast terahertz magnetometry. Nat. Commun. 11, 4247 (2020).
- 47. Zhang, S. *et al.* Nonrelativistic and nonmagnetic terahertz-wave generation via ultrafast current control in anisotropic conductive heterostructures. *Adv. Photonics* **5**, 056006 (2023).
- 48. Wang, P. *et al.* Inverse orbital Hall effect and orbitronic terahertz emission observed in the materials with weak spin-orbit coupling. *npj Quantum Mater.* **8**, (2023).
- 49. Ning, X. *et al.* Orbital Diffusion, Polarization, and Swapping in Centrosymmetric Metals. *Phys. Rev. Lett.* **134**, 026303 (2025).
- 50. Veneri, A., Rappoport, T. G. & Ferreira, A. Extrinsic Orbital Hall Effect: Orbital

- Skew Scattering and Crossover between Diffusive and Intrinsic Orbital Transport. *Phys. Rev. Lett.* **134**, 136201 (2025).
- 51. Liu, H. & Culcer, D. Dominance of Extrinsic Scattering Mechanisms in the Orbital Hall Effect: Graphene, Transition Metal Dichalcogenides, and Topological Antiferromagnets. *Phys. Rev. Lett.* **132**, 186302 (2024).
- 52. Tang, P. & Bauer, G. E. W. Role of Disorder in the Intrinsic Orbital Hall Effect.

  Phys. Rev. Lett. 133, 186302 (2024).
- 53. Liu, Q. & Zhu, L. Absence of orbital current torque in Ta/ferromagnet bilayers. arxiv.org/pdf/2501.10260 1–6 (2025).
- 54. Feng, Z. *et al.* Anomalous Nernst Effect Induced Terahertz Emission in a Single Ferromagnetic Film. *Nano Lett.* **23**, 8171–8179 (2023).
- 55. Zhang, H. *et al.* Tuning terahertz emission generated by anomalous Nernst effect in ferromagnetic metal. *Appl. Phys. Rev.* **10**, 021417 (2023).
- 56. Malinowski, G. *et al.* Control of speed and efficiency of ultrafast demagnetization by direct transfer of spin angular momentum. *Nat. Phys.* **4**, 855–858 (2008).
- 57. Bass, J. & Jr, W. P. P. Spin-diffusion lengths in metals and alloys, and spin-flipping at metal/metal interfaces: an experimentalist's critical review. *J. Phys. Condens. Matter* **19**, 183201 (2007).
- 58. Lu, W. T. & Yuan, Z. Spin accumulation and dissipation excited by an ultrafast laser pulse. *Phys. Rev. B* **104**, 214404 (2021).
- 59. Jackson, J. D. Classical Electrodynamics. (American Association of Physics

- Teachers, 1999).
- 60. Ordal, M. A., Bell, R. J., Alexander, R. W., Newquist, L. A. & Querry, M. R. Optical properties of Al, Fe, Ti, Ta, W, and Mo at submillimeter wavelengths.
  Appl. Opt. 27, 1203 (1988).
- 61. Polyanskiy, M. N. Refractiveindex.info database of optical constants. *Sci. Data* **11**, 94 (2024).
- 62. Tselin, A. *et al.* Exploring the dielectric function of platinum. *Phys. Rev. B* **110**, 195130 (2024).
- 63. Duvillaret, L., Garet, F. & Coutaz, J. L. A reliable method for extraction of material parameters in terahertz time-domain spectroscopy. *IEEE J. Sel. Top. Quantum Electron.* **2**, 739–745 (1996).
- 64. Gao-Fang, L. *et al.* Properties of Terahertz spectral in aluminium oxide crystal[J]. *J. Infrared Millim. Waves* **40**, 38–43 (2021).
- 65. Laman, N. & Grischkowsky, D. Terahertz conductivity of thin metal films. *Appl. Phys. Lett.* **93**, 051105 (2008).
- 66. Walther, M. *et al.* Terahertz conductivity of thin gold films at the metal-insulator percolation transition. *Phys. Rev. B* **76**, 125408 (2007).